Hindawi
Journal of Nanomaterials
Volume 2018, Article ID 4906746, 12 pages
https://doi.org/10.1155/2018/4906746

Research Article

Exploring the Capability of HAADF-STEM Techniques to Characterize Graphene Distribution in Nanocomposites by Simulations

N. Baladés,[1,2] **D. L. Sales**,[1,2] **M. Herrera**,[1,2] **A. M. Raya**,[1,3] **J. C. Hernández-Garrido**,[1,2] **M. López-Haro**,[1,2] **and S. I. Molina**[1,2]

[1]*Departamento de Ciencia de los Materiales e Ingeniería Metalúrgica y Química Inorgánica, Facultad de Ciencias, Universidad de Cádiz, Campus Río San Pedro s/n. 11510 Puerto Real, Cádiz, Spain*
[2]*Instituto Universitario de Investigación en Microscopia Electrónica y Materiales (IMEYMAT), CEI·MAR, Universidad de Cádiz, 11510, Puerto Real, Cádiz, Spain*
[3]*Instituto de Micro y Nanotecnología, IMN-CNM, CSIC (CEI UAM+CSIC), Isaac Newton, 8, E-28760, Tres Cantos, Madrid, Spain*

Correspondence should be addressed to N. Baladés; nuria.balades@uca.es

Received 23 July 2018; Revised 28 September 2018; Accepted 15 October 2018; Published 16 December 2018

Academic Editor: Ovidiu Ersen

This paper explores the capability of scanning transmission electron microscopy (STEM) techniques in determining the dispersion degree of graphene layers within the carbon matrix by using simulated high-angle annular dark-field (HAADF) images. Results ensure that unmarked graphene layers are only detectable if their orientation is parallel to the microscope beam. Additionally, gold-marked graphene layers allow evaluating the dispersion degree in structural composites. Moreover, electron tomography has been demonstrated to provide truthfully 3D distribution of the graphene sheets inside the matrix when an appropriate reconstruction algorithm and 2D projections including channelling effect are used.

1. Introduction

The usage of composite materials for industrial applications has dramatically increased since the late twentieth century. Particularly, the transport industry is continuously demanding new materials able of reducing structural weight improving performance in service [1, 2]. Aircraft manufacturers have steadily increased their relative usage of composites over the years, representing nowadays more than 50% by weight in some aircrafts [3]. One of the aimed developments for aircraft structural components is the production of nanoreinforcements that would provide antistatic properties to polymer matrix composite parts, in order to achieve electromagnetic shielding [4, 5]. To act as a shield that avoids electromagnetic interferences (EMI) such as reflection and/or adsorption of electromagnetic radiation by the devices during their useful life, an electrically conducting material with a balanced combination of conductivity, dielectric permittivity, and magnetic permeability is required. Compared with conventional metal-based EMI shielding materials, conducting polymer composites are lightweight, resistant to corrosion, and flexible and offer processing advantages [6]. Graphite, carbon black, and carbon fibre were the first to be combined with polymer to obtain EMI shields [7–9]. However, the EMI shielding effectiveness (SE) mainly depends on the intrinsic conductivity, the dielectric constant, and the aspect ratio of the composite material [6]. In this line, a graphene two-dimensional one-atom-thick material formed by a layer of carbon atoms in a densely packed hexagonal lattice offers a variety of intriguing attributes. Among others are a high electron mobility at room temperature (250,000 $cm^2/V{\cdot}s$) [10, 11], exceptional thermal conductivity (5000 $W/m{\cdot}K$) [12], superior mechanical properties, Young's modulus of 1 TPa, and fracture strength of 125 GPa [13]. Furthermore, this novel material has also an almost constant electrical permittivity over three decades of frequency, in a

range from 10 to 40 GHz [14]. These characteristics, together with large aspect ratio and high electrical conductivity, would provide an extraordinary EMI shielding effectiveness in the resulting composite [15–17]. This profile of material features makes graphene an ideal nanoreinforcement of polymers in aerospace applications [18, 19].

Despite their unique characteristics, to achieve high homogeneity graphene dispersion within the polymer matrix is still a challenge to overcome [20–23]. The high cohesive force between graphene sheets and the weak interaction among graphene and polymer matrix limit their usage in typical industrial batch sizes. One possibility to face this problem is disrupting the bonding between graphene sheets by functionalizing the graphene surface [24]. For that reason, various chemical routes have been proposed to incorporate a huge number of suitable atoms/organic groups on graphene sheets [25]. However, to achieve the best performance of the resultant graphene-functionalized polymer, a strict interface control and an adequate dispersion degree are required. So, an important task to enable progress on this advanced nanocomposite is to control both dispersion degree and orientation of the modified graphene sheets into the polymer matrix at atomic scale. In this sense, we propose HAADF-STEM techniques to trace nanolayer distribution. When a focused beam scans a sample and the electrons scattered at high angles are collected, the resultant intensity signal in the detector is approximately proportional to the square of the average atomic number ($\bar{Z}^2$), allowing to extract structural and compositional information at sub-angstrom level.

During the past few decades, several materials have been characterized by using HAADF-STEM techniques [26–28]. It is worth mentioning that the characterization of carbonaceous materials through this technique is more challenging. The presence of carbon in both materials - graphene and polymer matrix - does not offer contrast enough in the resultant HAADF-STEM image. However, despite the low atomic number of carbon, this imaging technique has been used, for example, to count the number of graphene layers of stacked graphene sheets [29]. As this technique is a very useful one for locating high atomic-number materials surrounded by a light matrix, we suggest the marking of functionalized graphene sheets with a heavy metal such as gold to improve contrast in the formed HAADF-STEM image. Experimentally, because of the low chemical activity of pristine graphene, the presence of oxygen functionalities at the graphene surface provides reactive sites for the nucleation and growth of different metallic particles [30]. An example of individual gold atoms detected in a few graphene layers with this technique can be found in [31]. Furthermore, HAADF-STEM also allows electron tomography to 3D reconstruction of atomic structures, when a proper microscope holder is used. This Z-contrast technique has been previously used to reconstruct gold nanoparticles deposited on amorphous carbon [32] or platinum nanoparticles on a carbon nanofiber [33]. Other chemical analyses through TEM-techniques at nanometre scale, such as electron energy-loss spectroscopy (EELS) or energy-dispersive X-ray spectroscopy (EDX), are not considered in this work because they require longer exposition time to the electron beam, causing large radiation damage in the studied sample.

Table 1: Graphite and diamond structures.

Structure	Graphite	Diamond
Hybridization	sp^2	sp^3
Bond distance (nm)	0.142	0.154
Neighbours	2	3
Bond angle	120°	109°
Density (g/cm^3)	2.26	3.52

The aim of this work is to explore the capability of the HAADF-STEM technique in determining the state of dispersion of graphene sheets within polymer matrices. In order to contribute to the optimization of possible manufacturing techniques, with the support of atomic structure models and their corresponding simulated HAADF-STEM images, we propose methods to obtain information about the 3D dispersion degree of graphene sheets within amorphous carbon.

2. Simulation Details

2.1. Modelling. In this work, several atomic structures were generated by using MATLAB software. These models consist of portions of amorphous carbon matrices encircling unmarked or gold-marked graphene sheets at different orientations.

Graphene sheets were modelled as monolayers of sp^2-hybridized carbon atoms ($Z = 6$) arranged in a two-dimensional hexagonal lattice, taking into account the atomic bond conditions shown in Table 1 [34]. For the case of gold-marked functionalized graphene sheets, the most stable adsorption site without breaking the graphene structure corresponds to an adsorption site located over the carbon atoms that form the hexagonal ring, known as the T-site position. In this configuration, the bond energy Au-C is 0.8 eV and the migration energy of Au over the graphene sheet is only 0.03 eV, which allows keeping gold atoms attached to carbon atoms with a bond distance of 0.241 nm [35, 36].

Amorphous carbon is a noncrystalline carbon containing a mixture of diamond (sp^3-hybridized carbon atoms) and graphite (sp^2-hybridized carbon atoms) crystal structures, whose characteristics are summarized in Table 1. The amorphous carbon materials' properties usually lie between diamond and graphite ones [37]. With a relatively large proportion (65%) of diamond-like sp^3 bonds between pairs of carbon atoms and a relatively small proportion (35%) of graphite-like sp^2 bonds, the resultant material can be considered amorphous rather than crystalline [38]. In this line, an amorphous carbon matrix formed by 65% of diamond and 35% of graphite has been modelled considering the number of neighbouring atoms, bond angles, and bond distances given by the hybridization type and the pondered average density, which confers certain short-range order upon this amorphous material.

Different models described in each section have been used to explore the capability of HAADF-STEM techniques

Table 2: Settings used for multislice simulations.

Acceleration voltage	100 kV
Aberration coefficient C_3	$1.545 \cdot 10^{-5}$ m
Aberration coefficient C_5	-0.01259 m
Objective aperture angle	32 mrad
HAADF inner collection angle	70 mrad
HAADF outer collection angle	210 mrad
Defocus	0 m
Pixel size	$2\ 10^{-12}$ m

in determining graphene sheet location, dispersion, and orientation within an amorphous carbon matrix. Although, these models might not result in a chemically realistic structure, they offer sufficient accuracy for image simulation and analysis purposes.

2.2. Image Simulation. Simulated HAADF-STEM images of these models have been obtained by using SICSTEM simulation software [39]. This algorithm uses a parallel implementation of the multislice method [40]. SICSTEM runs on the CAI cluster composed of 80 nodes, each biprocessor node having a double core and 640 Gb of main memory, achieving a peak performance of 3.8 TFlops (billions of floating point operations per second) [41]. SICSTEM takes into account thermal diffuse scattering (TDS) in the calculation of the intensity in the object exit plane. The simulation settings are summarized in Table 2. Though it is well known that graphene is very sensible to the beam-sample interactions and experiments should be carried out at lower voltages [42], we have used 100 kV in order to obtain good-quality images.

2.3. Tomography Simulation. To compute a volume through electron tomography, four main steps are required: acquisition of a series of 2D projections at different tilt angles (tilt-series data), image alignment, reconstruction, and visualization. It is worth mentioning that the tomogram's resolution is degraded by missing information as a consequence of the specimen tilt range and finite tilt increments. As each 2D projection corresponds to a plane of information in reciprocal space, specimens with needled shape geometry permit the full 180° tilt range. However, practical limitations, such as the sample in itself and the specimen holder's geometry, normally restrict the tilt range to less than ±70°.

In our particular cases, each 2D projection corresponds to one simulated HAADF-STEM image of the atomic model shown in Figure 1 at a specific view angle. Concretely, a tilt-series of 73 2D projections was acquired by rotating the model at equal-slope increment of 2.5° along the *y-axis*. The tilt-series data was viewed with ImageJ processing free software [43]. The alignment and reconstruction processes of the tomographic series were performed by using TomoJ, an ImageJ plug-in. The tomographic reconstruction of the simulated tilt-series data were performed using two algorithms: the simultaneous iterative reconstruction technique (SIRT) [44] and the compressed sensing-based algorithm (CS) for the total variation minimization (TVM) technique [45]. The SIRT algorithm is an iterative method based on the algebraic reconstruction technique. 100 iterations and a relaxation coefficient of 1 were selected [46]. The CS allows reducing considerably the amount of data necessary for the reconstruction of the final volume. In the field of CS, an underestimated system of equations can lead to an exact solution if the signal (or an expression of the signal in another basis) is sparse enough. In the case of electron tomography, this effect can be present in the gradient of the signal. Thus, when this prior knowledge is exploited, the algorithms based on TVM can be used. To carry out TVM reconstruction, the TVAL3 solver was used [47]. A regularization parameter (μ) equal to 2^7 was considered. The reconstructions were implemented in MATLAB using ASTRA Toolbox [48]. The tomograms were then rendered and analysed using AVIZO 3D-viewing software.

3. Results and Discussion

To analyse the possibility of displaying graphene sheets inside polymeric nanocomposites, atomic models representing a piece of amorphous carbon about 150 nm^3 in volume were generated. In each model, the graphene sheets vary in orientation in relation to the incident electron probe. Subsequently, the HAADF-STEM images of the models were simulated. Figure 2(a) shows the atomic model that represents a matrix of amorphous carbon (green colour) that surrounds three graphene sheets perpendicularly oriented to the electron beam (blue colour). The corresponding simulated HAADF-STEM image is shown in Figure 2(b). As it was expected, given by the similar chemical nature of the amorphous carbon and graphene sheets, it is hard to determine the graphene sheet location. Nevertheless, in the case where the graphene sheet is oriented along the electron beam of the microscope (as it is shown in the model of Figure 2(c)), its position inside the amorphous matrix is clearly detected in the resultant HAADF-STEM image (Figure 2(d)), registering a much stronger contrast than the amorphous carbon alone. In order to compare the differences of the intensity values, a comparison between intensity profiles taken from both images is shown in Figure 2(e). The selected integration areas have been marked in the simulated HAADF-STEM images with blue and red rectangles, respectively. As it can be appreciated, due to the random orientation of the carbon atoms inside the amorphous matrix, the intensity value depends on the number of carbon atoms that cross the beam. Therefore, the area of the image where the three sheets of the model are located in Figure 2(b) slightly increases the intensity value (~10%) with respect to the area free of graphene. However, when the graphene sheet is oriented parallel to the electron beam, the given HAADF-STEM intensity is about 70% higher than any other orientation, allowing its right visualization. This happened as a clear consequence of the so called channelling effect. This phenomenon typically occurs when the electron beam interacts with crystalline solid at certain angles, in which the path of charged particles is constrained and individual acts of dispersion are turned into a cooperative effect. Channelling is enhanced in this 2D material when the surface of the graphene sheet is oriented

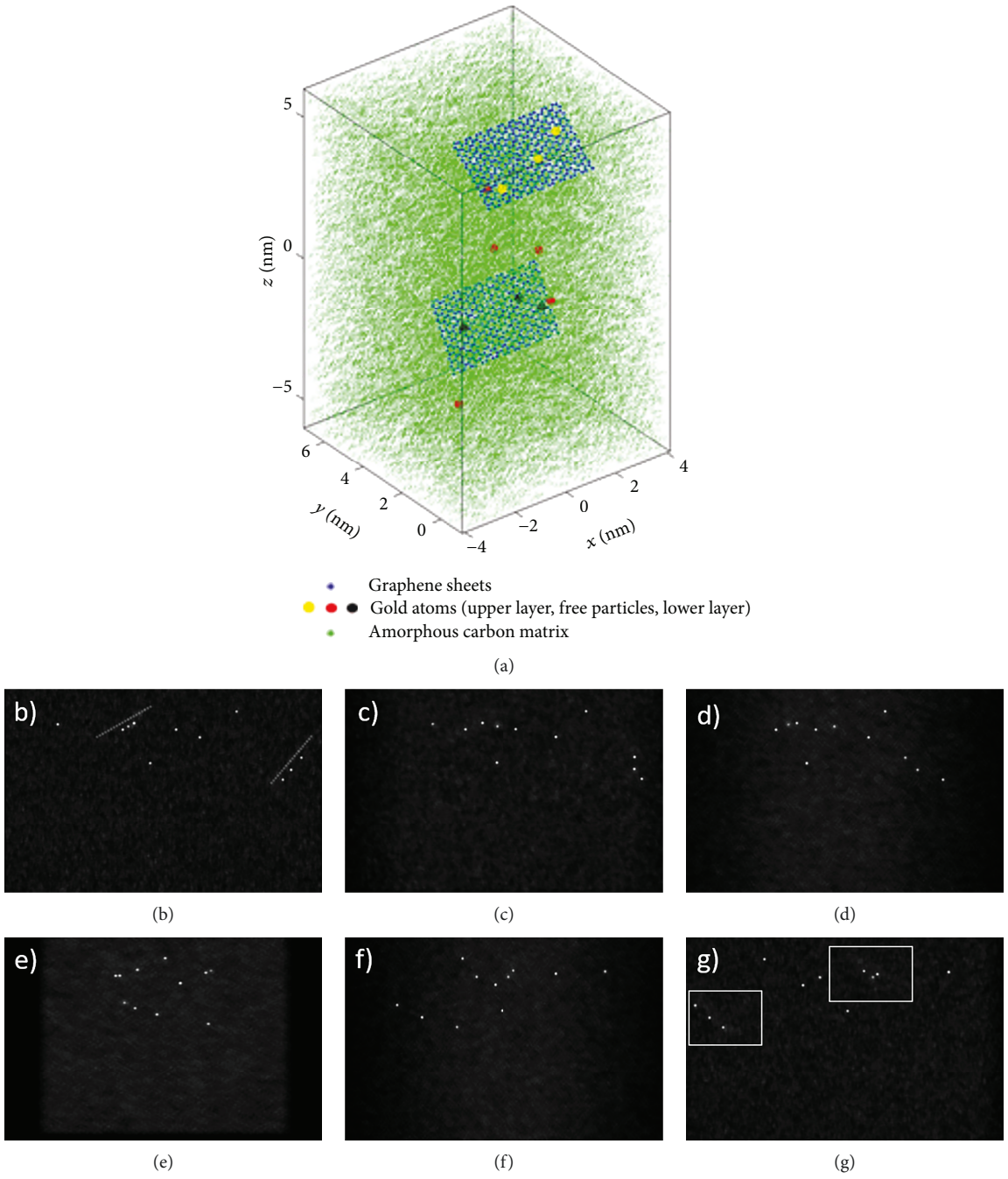

FIGURE 1: (a) Atomic model for the tomography study. HAADF-STEM-simulated images at different tilt angles with respect to the beam direction along the *y-axis*: -90° (b), -70°(c), -45° (d), 0° (e), 45° (f), and 82.5° (g). Graphene sheets can be detected within the amorphous matrix only in the tilted 2D projections which are almost parallel to the beam direction. In Figure 1(b), graphene layers are perfectly distinguished, and in Figure 1(g) their position - marked with white squares - can be estimated.

along the electron beam, because this configuration allows a larger fraction of electrons being dispersed at higher angles, so image intensity is increased.

Once the difficulty of locating graphene sheets by *Z*-contrast imaging is exposed, new models with gold atoms added to the graphene surface are considered in order to increase the intensity in the resultant HAADF-STEM images. In this sense, Figure 3(a) shows an atomic model representing a piece of amorphous carbon of about 200 nm^3 in volume encircling two gold-marked graphene layers. Its corresponding simulated HAADF-STEM image is in Figure 3(b). As it can be observed, gold atoms are clearly identified as peaks of intensity in the HAADF-STEM image (Iz). In addition, the gold atoms of the same graphene sheet, i.e., located at equal height (z) inside the amorphous carbon, give the same intensity value. Furthermore, a constant intensity variation has been measured when gold-marked graphene layers are leaning. To better illustrate that effect, an atomic model

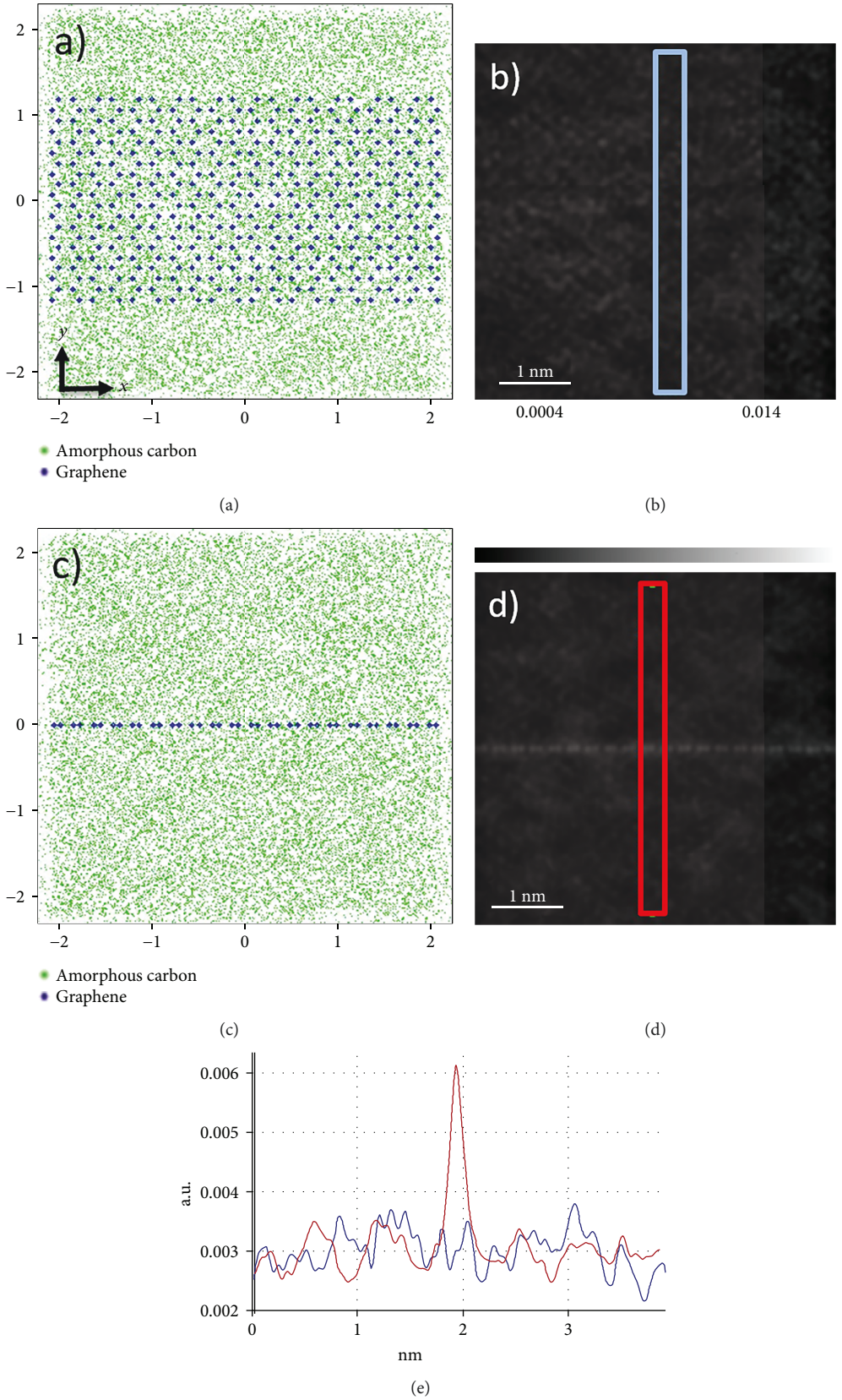

FIGURE 2: 2D projection in the *xy-plane* of different pristine graphene sheets leaning within the amorphous carbon matrix: (a) three graphene sheets perpendicularly oriented to the beam direction; (c) a graphene sheet perpendicular to the *xy-plane*. (b, d) Simulated HAADF-STEM images of the models shown in (a) and (c), respectively. (e) Intensity profiles taken along the blue and red rectangles marked in (b) and (d).

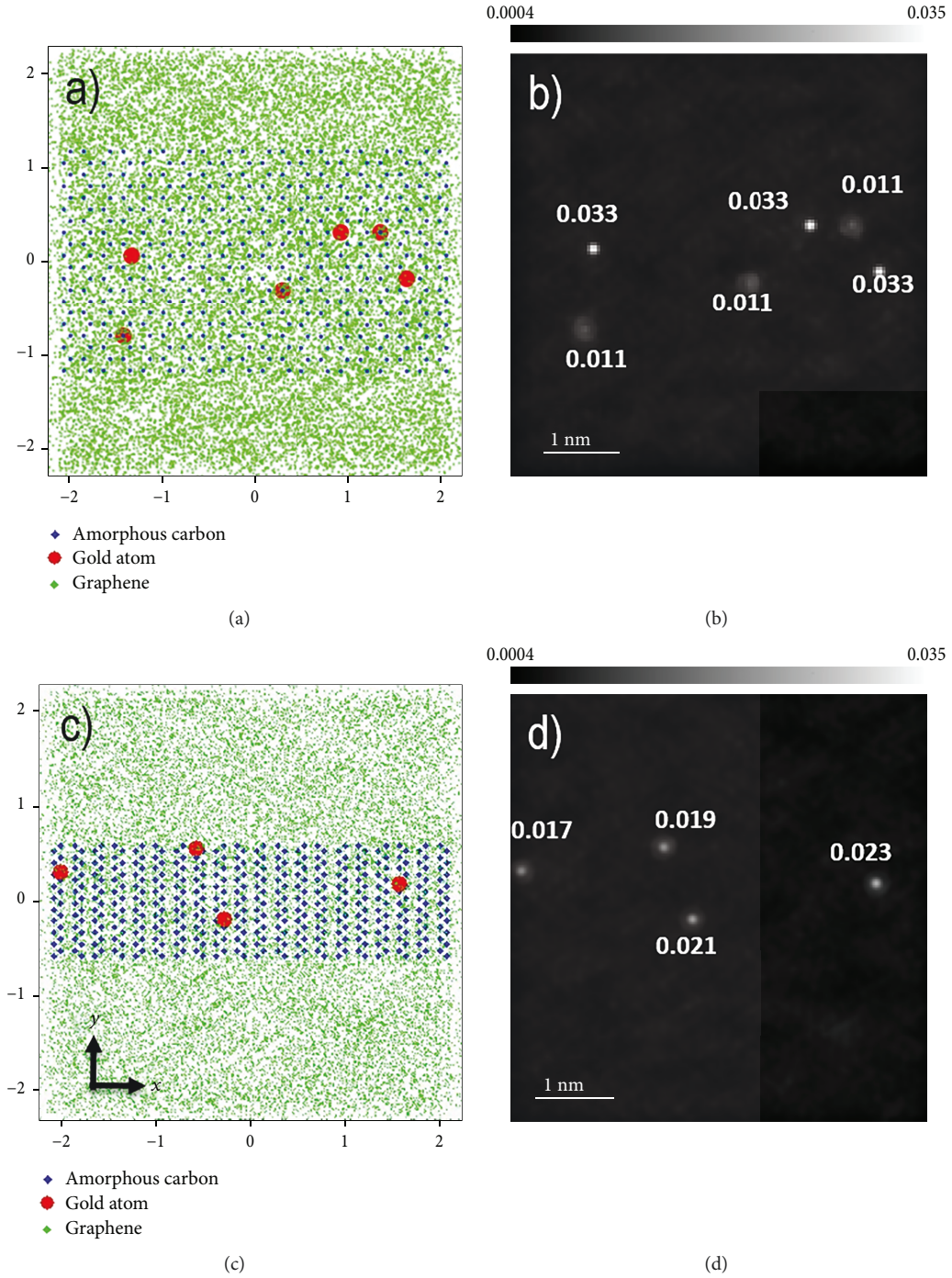

Figure 3: 2D projection in the *xy-plane* of the different gold-marked graphene sheets sloping within the amorphous carbon matrix: (a) two graphene sheets perpendicularly oriented to the beam direction; (c) a graphene sheet 60° oriented to the *xy-plane*. (b, d) Simulated HAADF-STEM images of the models shown in (a) and (b), respectively.

representing a graphene sheet 60° oriented with respect to the *xy-plane* within the amorphous carbon matrix and its corresponding simulated HAADF-STEM image are shown in Figures 3(c) and 3(d), respectively. As it can be seen, the maximum intensity value associated to a gold atom changes slightly from the one nearby. However, a gradual intensity variation related to the *z*-gold atom position is clearly appreciated when comparing intensity values among them ($\Delta Iz \sim 0.002$ units). These results point out a linear correlation between HAADF-STEM intensity and graphene layer sloping. On the one hand, when graphene sheets are oriented parallel to the *xy-plane*, all gold atoms over the surface have the same HAADF-STEM intensity value (i.e., when these values are compared one to each other: $\Delta Iz = 0$). On the other hand, when the sheet is sloping to the *xy-plane*, the HAADF-STEM intensity peaks increase or decrease

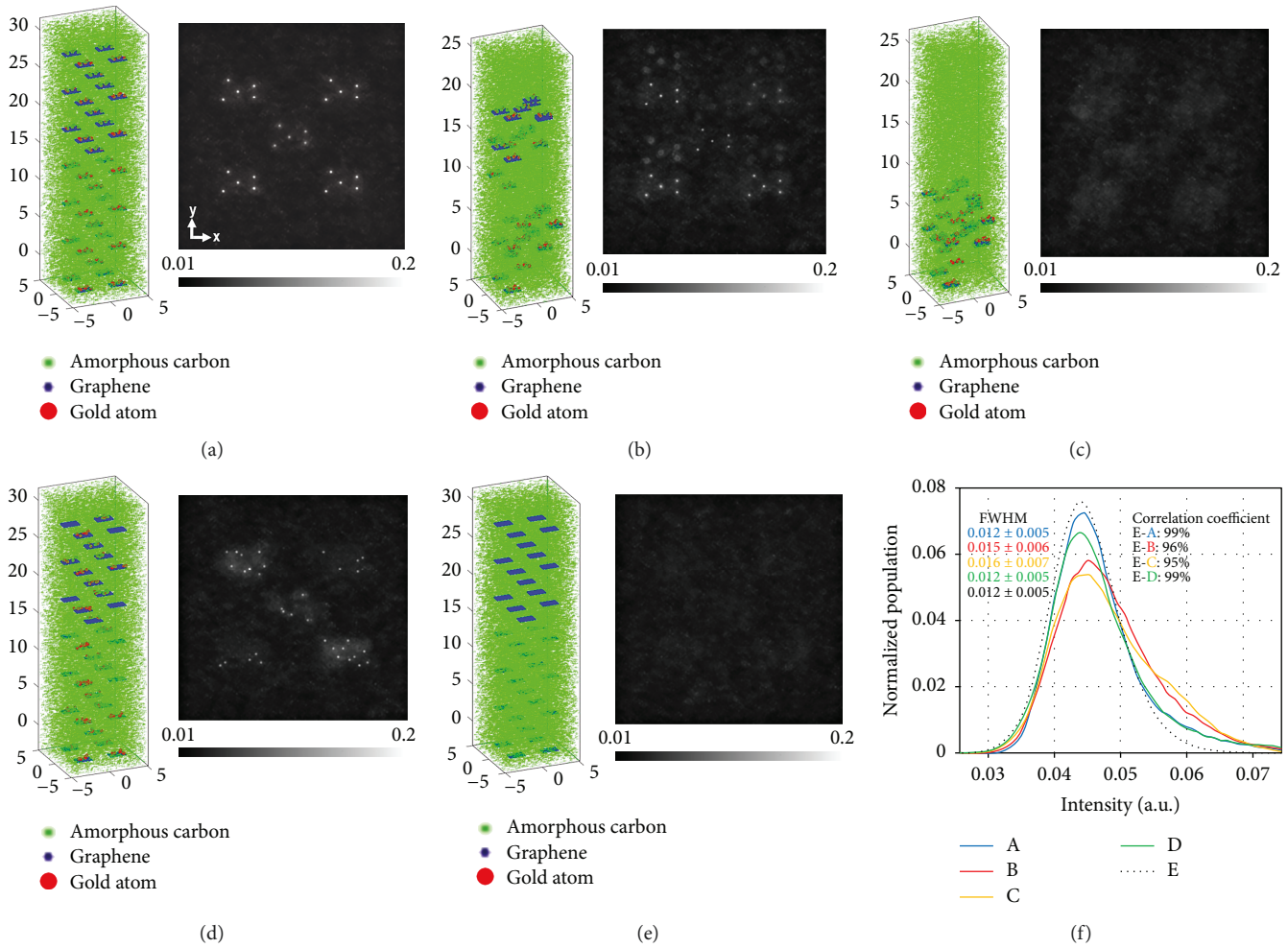

Figure 4: Atomic models (dimension in nm) exemplifying different dispersion degrees in structural graphene-based composites and their simulated HAADF-STEM images: gold-marked (a) and unmarked (e) graphene sheets homogeneously dispersed within the amorphous matrix. Two graded inhomogeneous dispersion models: random dispersion model (b) and a grouped one (c). A homogeneous model consists of unmarked graphene layers (d). (f) Fitted probability distribution graphs. FWHM of the curves and correlation coefficients are shown in the image.

progressively depending on its 3D location (i.e., when the intensity of different gold atoms is compared among them: $\Delta Iz = \text{constant}$). As gold peak intensity values depend not only on sheet height but also on their relative inclination with respect to the *xy-plane*, dissimilar graphene dispersion configurations may agree with the same intensity image contrast. Therefore, when the orientation of graphene sheets is not known beforehand, it is not possible to accurately guess it only by observing peaks of intensity values in HAADF-STEM images.

In case of structural materials in which graphene sheets need to maintain a similar alignment within the matrix [49], the sensibility of HAADF-STEM intensity values to the position of gold atoms may be used as a way to know the dispersion degree of the graphene sheets. For that, we investigated whether the changes in graphene dispersions are somehow noticeable by image histograms, the statistical graph of the frequency distribution of the HAADF-STEM image intensity values. We consider histograms because they are easily obtained.

Figure 4 shows the atomic models used in this study together with their corresponding simulated HAADF-STEM images. Specifically, they consist of a piece of amorphous matrix of about 3000 nm^3 containing 1% of graphene filler. The graphene sheets have been distributed in a way that represents different dispersion states: (a) a homogeneous gold-marked dispersion model; (b) a random dispersion one, which represents gold-marked graphene sheets distributed without any predictable pattern; (c) a grouped one, representing a model in which gold-marked sheets are accumulated in specific zones and there are areas without filling. In addition, a model representing a homogeneous dispersion containing marked and unmarked graphene sheets is shown in (d). Finally, a uniform unmarked graphene model is included as reference in (e). Although nowadays in real composites the sheets may not be as perfectly positioned as those in the model are, there are manufacturing techniques being currently developed to achieve this [50, 51].

To be able to compare the resulting histograms from images in Figure 4, firstly we have changed all histograms

into the same bin size and the number of pixels in every image was normalized. Then, to achieve a more accurate measurement of the intensity distribution in the HAADF-STEM images, the histograms were fitted to probability graphs, concretely to a simple Gaussian distribution. Figure 4(f) shows the probability distribution graphs of the intensity data corresponding to the HAADF-STEM images shown in Figure 4. Under the established imaging conditions in Table 2, results disclose a bell-shaped and symmetric data distribution for the unmarked model (black dashed line), meaning that intensity variation in the simulated image is built up of many independent small causes of variation, the carbon atom distribution in the atomic model. Moreover, in this case the mean intensity value (0.045 a.u.) and the standard deviation (0.006) are the lowest ones, meaning that most of the intensity values are close to the mean one. This happens because most of pixels in the HAADF-STEM image are formed after the interaction of the beam probe with barely the same number of carbon atoms, giving as a result similar intensity values. However, in gold-marked models (a-d) the typical Gauss bell changes towards a right-tailed intensity distribution. In the case of gold-marked graphene layers, because of the presence of heavy atoms, the population of pixels brighter than the mode increases, tending the histogram to be skewed to the right. Results also disclose a reduction in the curve height together with an increment in the full width at half maximum (FWHM) as graphene sheets get more stacked, decreasing their correlation with the unmarked model (shown as inset in Figure 4(f)). So, observing the fitted graphs, it is relatively easy to distinguish among a homogeneous graphene layers distribution (blue and green curves) from an intercalated distribution (red curve) and a stacked one (yellow curve). These results suggest that HAADF intensity image histograms are somehow sensible to sheet dispersion. For example, the HAADF-STEM simulated image of an unmarked but homogeneously dispersed model (e) depicts a very similar contrast to the one presented by the marked graphene but heavily stacked (c). Nevertheless, the shape of their resultant Gauss curves is dissimilar enough to distinguish both graphene sheet distribution inside the amorphous carbon.

Though histograms may provide some qualitative information about graphene distributions, these curves and their related HAADF-STEM images (due to their 2D nature) offer enough information to establish the volumetric dispersion of graphene layers inside the matrix, as needed in case of nanocomposites for electrical applications. In the graphene-based nanocomposites, to improve electrical properties in the resultant composites, a random distribution of graphene layers is essential to achieve a better interconnection among graphene layers [52].

To solve this matter, a HAADF-STEM tomography study was carried out using the atomic model described in Figure 1. Additionally, to gain more insight concerning the feasibility of electron tomography for the visualization of the graphene layers inside the matrix, three different scenarios were considered. In particular, we have investigated the effect of (i) the number of projections over a maximum tilt range, (ii) the limit tilt range, and (iii) the influence of the angular sampling $(\Delta\theta) = 2.5^\circ$ and 5°. For the limited tilt range, we simulated a tilt series from -90° to $+50^\circ$, containing projections with graphene sheets well oriented, and tilt series from -70° to $+70^\circ$. Note that in this case, the graphene sheets are disoriented. Additionally, all these scenarios were reconstructed using SIRT and TVM algorithms. The HAADF-STEM tilt series movie-file, from a maximum tilt range every 2.5°, is shown in Supporting Information (Movie 1). From this aligned file, the rest of the schemes are extracted to be reconstructed.

Figure 1 shows the atomic model used for the tomographic study, consisting of 119,467 atoms, representing a compound of 700 nm^3, consisting of an amorphous carbon matrix encircling two graphene sheets. The graphene sheets are marked with gold atoms. The upper layer is tilted 30° and the lower one 50° with respect to the *y-axis*. The model includes five randomly dispersed gold atoms. Simulated HAADF-STEM images of the model at different tilt angles are displayed at the right. Although graphene sheets are present in all 2D projections of the tilt series, they are only slightly visualized inside the amorphous matrix (white squares in Figure 1(g)) when the model is rotated with respect to the beam direction at high angles (values over $\pm 82^\circ$) and clearly detected at $\pm 90^\circ$ as it can be observed in Figure 1(b), because of the channelling effect described previously (see Supporting Information Movie 1).

Figure 5 shows slices extracted from the SIRT (first row) and the TVM (second row) reconstructions, respectively. The slices were perfectly oriented at the same plane of the upper graphene layer surrounded by the amorphous carbon matrix. For the best of the proposed acquisition scheme, 180° with 73 projections, both reconstruction algorithms enable the visualization of the graphene layer. However, in the SIRT reconstruction, streaking artefacts arising from the gold markers are present, reducing the quality for graphene/matrix contrast imaging. In the TVM reconstruction, these artefacts are less pronounced. For a better visualization of these artefacts caused by the gold markers, Figure 6 shows volume rendering of eight reconstructions. In the case of the SIRT algorithm (Figure 6(a)), the streaking artefacts are visibly along the *z-axis* with gold markers distorted from the original spherical morphology. But if the number of projections is reduced to 37, increasing the tilt increment $\Delta\theta$ from 2.5° to 5° (scheme 2), the streaking effects are more pronounced for SIRT reconstruction (Figures 5(b) and 6(b)). In contrast, TVM is less affected by the largest tilt increment and the contrast between the graphene and the matrix still remains acceptable (Figures 5(f) and 6(f)).

As the channelling effect influences the quality of the reconstructions, its influence is also evaluated for the schemes labelled as 3 and 4. For these acquisition schemes, the tilt range is limited to 140°. In scheme 3 with a tilt range from -90° to +50°, we are considering a tilt series with projections where the channelling effect is present and hence with a much stronger contrast than the amorphous carbon. For this case, in the SIRT reconstruction, in addition to streaking artefacts, an elongation in the direction of the missing wedge is present (Figures 5(c) and 6(c)). In the TVM reconstruction, these artefacts are less pronounced and practically did

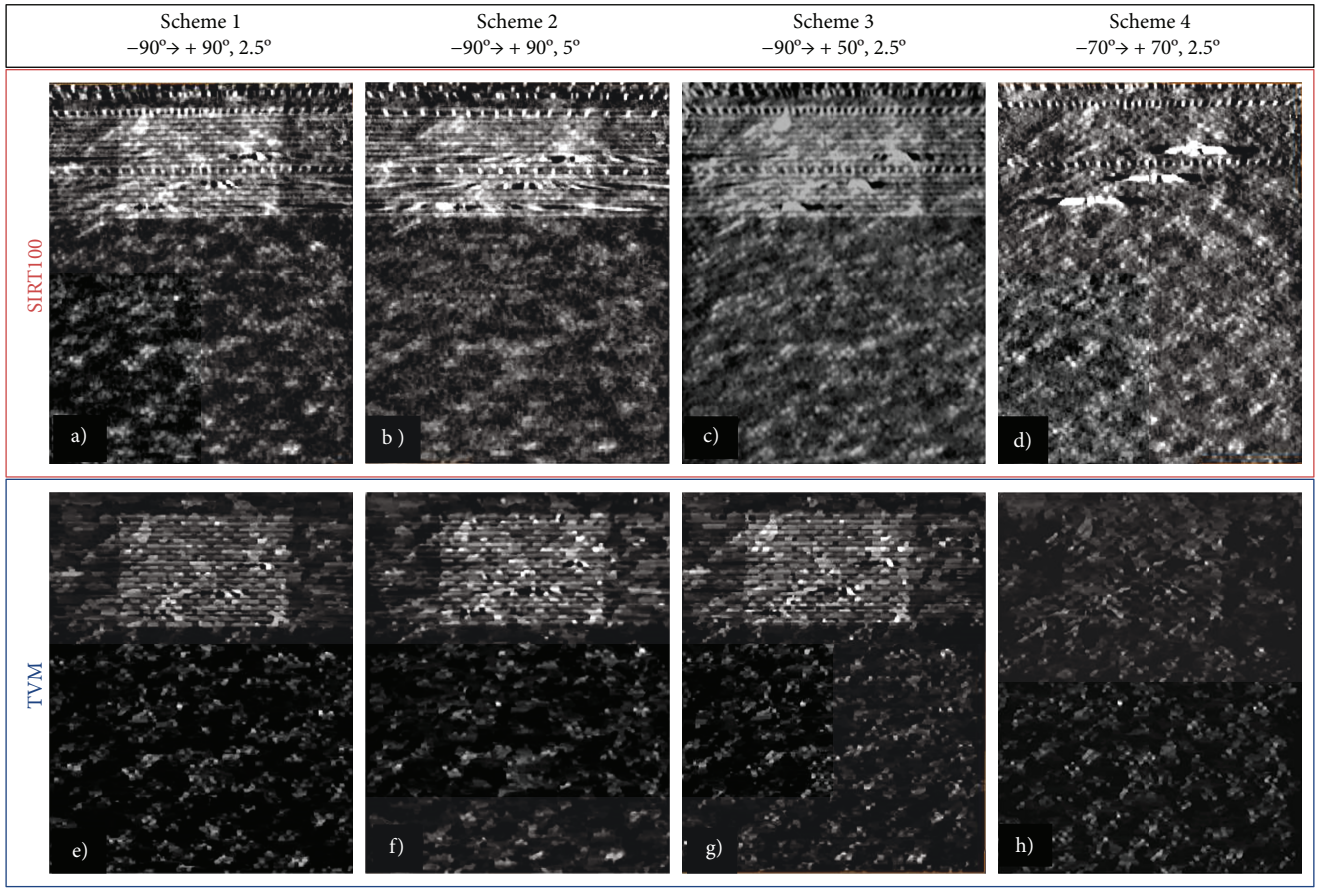

Figure 5: Reconstructed images by SIRT and TVM at different acquisition parameters. Slices through the SIRT (a–d) and TVM (e–h) reconstructions showing the upper graphene layer surrounded by the amorphous carbon.

not show differences from the previous better acquisition condition schemes (Figures 5(g) and 6(g)). Nevertheless, in the case where any of the projections used to reconstruct the volume did not suffer from channelling effects, this is assumed in this work considering the tilt range between ±70° (scheme 4); the visualization of the graphene sheets dramatically decreases for both SIRT (Figures 5(d) and 6(d)) and TVM (Figures 5(h) and 6(h)). Results show that the appropriate tomographic 3D reconstruction of the model provides truthfully 3D distribution of the graphene sheets inside the matrix (see Figure 6 and Supporting Information Movie 2), being possible to check the method used to produce the nanocomposite, in order to manufacture homogeneous or inhomogeneous dispersion.

4. Conclusions

In summary, based on the results obtained from the simulations of the studied atomic models, we show that graphene sheets in organic composites are clearly identifiable by HAADF-STEM techniques when graphene layers are oriented in the direction of the electron beam, due to the channelling effect. In order to improve the contrast, we propose marking graphene sheets with heavy atoms, e.g., gold. To explore the chance of determining the dispersion degree in structural composites by using 2D-projected HAADF-STEM images, a statistical study is carried out in models representing three different dispersion states. Although in the image intensity probability graphs some differences are found among homogenous, intercalated, and stacked dispersions, the 2D nature of this technique does not allow an accurate correlation of the resultant intensity curve shape with the position and orientation of graphene sheets in case of interconnected graphene layers' distributions.

To overcome these limitations, an electron tomography study is proposed. Results from simulated HAADF-STEM electron tomography reveals that this technique is a successful one to identify and locate reinforced areas in nanocomposites and therefore a way of controlling graphene sheet dispersion. Moreover, we find that SIRT reconstruction is more affected by variations in the acquisition parameters like maximum tilt range and tilt increment. In contrast, TVM reconstruction significantly reduces noise and sharpens transitions between graphene sheets and the carbon matrix which will enable a simpler and easier segmentation of the reconstruction. Additionally, the TVM algorithm suffers less from the incomplete sampling in Fourier space due to the missing wedge and is not strongly affected from the lower number of projections. These advantages can be extremely useful for very sensible materials, like graphene, when quick tilt series

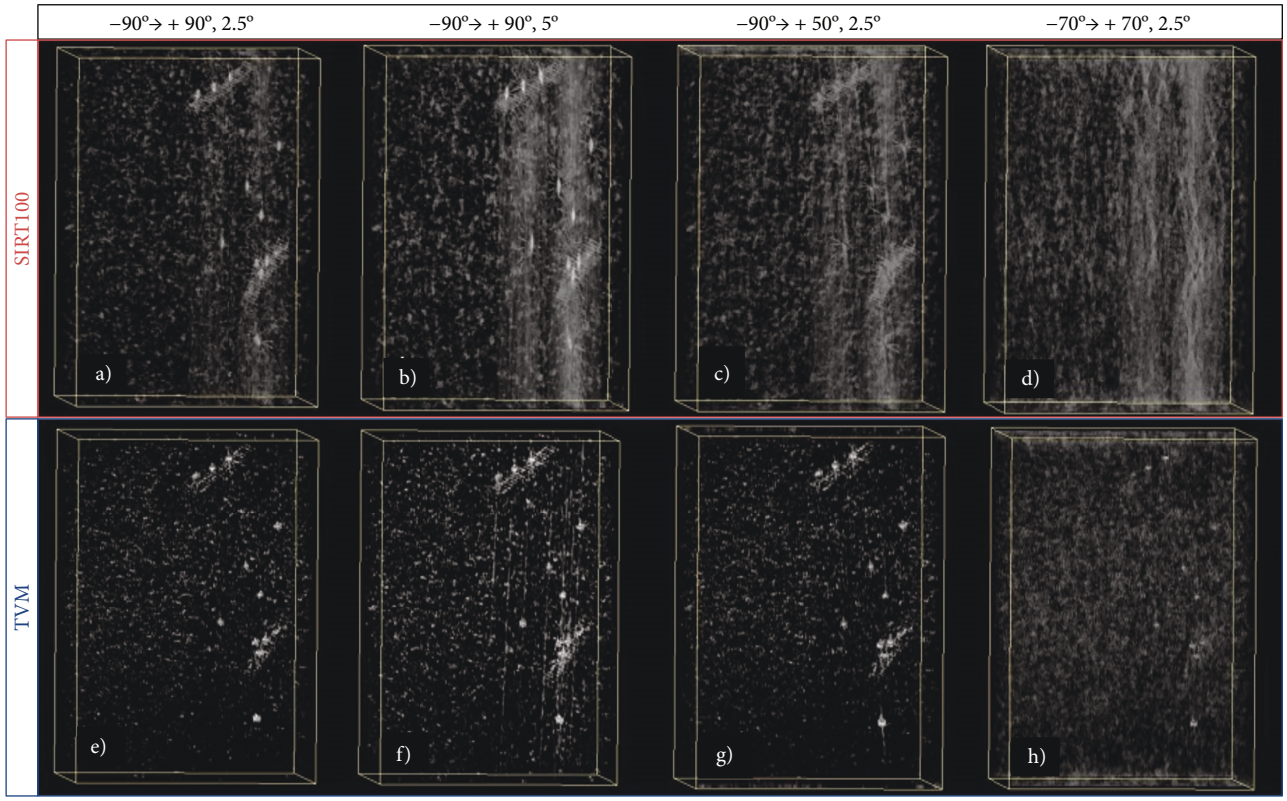

Figure 6: 3D rendering of the reconstructed SIRT and TVM images at different acquisition parameters. Volume rendering of reconstruction algorithms: SIRT (a–d) and TVM (e–h).

needs to be acquired to reduce beam-sample interactions even when low voltages are used. Expectedly, the fidelity of both reconstruction methods decreases when the channelling effect is dismissed. To avoid this in practice, the operator should select only those areas from which, tilting as much as possible according with their instrumental limitations, channelling effects on the HAADF-STEM images are detected.

Data Availability

The simulation detail data used to support the findings of this study are available from the corresponding author upon request.

Conflicts of Interest

The authors declare that they have no conflicts of interest.

Acknowledgments

This work was supported by the Spanish MINECO (projects TEC2014-53727-C2-2-R and TEC2017-86102-C2-2-R) and the Junta de Andalucía (PAI research groups TEP-946 INNANOMAT, TIC-145, and FQM334). Cofinancing from UE-FEDER is also acknowledged. J.C.H-G. acknowledges support from the Ramón y Cajal Fellowships Program of MINECO (RYC-2012-10004). M.L-H acknowledges support from the Juan de la Cierva Fellowships Program of MINECO (IJCI-2014-19367).

Supplementary Materials

The uploaded supplementary material as a .zip file includes two movies showing 3D visualization of the 2D projections at different angles related to the model used by tomography study (Movie 1) and the reconstruction of the same model using two algorithms TVM and SIRT (Movie 2). Similar images shown in the article have been taken from these movies. *(Supplementary Materials)*

References

[1] E. C. Claunch, "Forecasting on composites-markets, products and demands," *Journal of Textile and Apparel, Technology and Management*, vol. 9, no. 2, 2015.

[2] S. Arabab, "Research in carbon-carbon composites," in *Open SIUC*, Spring, 2015.

[3] http://www.airbus.com/innovation/proven-concepts/in-design/innovative-materials/.

[4] D. D. L. Chung, "Electromagnetic interference shielding effectiveness of carbon materials," *Carbon*, vol. 39, no. 2, pp. 279–285, 2001.

[5] S. Dasgupta, "Polymer matrix composites for electromagnetic applications in aircraft structures," *Journal of the Indian Institute of Science*, vol. 95, no. 3, pp. 275–296, 2015.

[6] M. B. Bryning, M. F. Islam, J. M. Kikkawa, and A. G. Yodh, "Very low conductivity threshold in bulk isotropic single-walled carbon nanotube-epoxy composites," *Advanced Materials*, vol. 17, no. 9, pp. 1186–1191, 2005.

[7] M. Crespo, M. González, A. L. Elías et al., "Ultra-light carbon nanotube sponge as an efficient electromagnetic shielding material in the GHz range," *Physica Status Solidi (RRL) - Rapid Research Letters*, vol. 8, no. 8, pp. 698–704, 2014.

[8] N. C. Das, D. Khastgir, T. K. Chaki, and A. Chakraborty, "Electromagnetic interference shielding effectiveness of carbon black and carbon fibre filled EVA and NR based composites," *Composites Part A: Applied Science and Manufacturing*, vol. 31, no. 10, pp. 1069–1081, 2000.

[9] J. M. Thomassin, C. Jérôme, T. Pardoen, C. Bailly, I. Huynen, and C. Detrembleur, "Polymer/carbon based composites as electromagnetic interference (EMI) shielding materials," *Materials Science and Engineering: R: Reports*, vol. 74, no. 7, pp. 211–232, 2013.

[10] K. S. Novoselov, A. K. Geim, S. V. Morozov et al., "Two-dimensional gas of massless Dirac fermions in graphene," *Nature*, vol. 438, no. 7065, pp. 197–200, 2005.

[11] K. S. Novoselov, A. K. Geim, S. V. Morozov et al., "Electric field effect in atomically thin carbon films," *Science*, vol. 306, no. 5696, pp. 666–669, 2004.

[12] A. A. Balandin, S. Ghosh, W. Bao et al., "Superior thermal conductivity of single-layer graphene," *Nano Letters*, vol. 8, no. 3, pp. 902–907, 2008.

[13] C. Lee, X. Wei, J. W. Kysar, and J. Hone, "Measurement of the elastic properties and intrinsic strength of monolayer graphene," *Science*, vol. 321, no. 5887, pp. 385–388, 2008.

[14] A. Cismaru, *Microwave and Millimeterwave Electrical Permittivity of Graphene Monolayer*, C. University, 2013.

[15] J. Liang, Y. Wang, Y. Huang et al., "Electromagnetic interference shielding of graphene/epoxy composites," *Carbon*, vol. 47, no. 3, pp. 922–925, 2009.

[16] C. Acquarelli, A. Rinaldi, A. Tamburrano, G. De Bellis, A. G. D'Aloia, and M. S. Sarto, "Graphene-based EMI shield obtained via spray deposition technique," in *2014 International Symposium on Electromagnetic Compatibility*, pp. 488–493, Gothenburg, Sweden, September 2014.

[17] V. Eswaraiah, V. Sankaranarayanan, and S. Ramaprabhu, "Functionalized graphene-PVDF foam composites for EMI shielding," *Macromolecular Materials and Engineering*, vol. 296, no. 10, pp. 894–898, 2011.

[18] S. Horacio, *Graphene-Based Polymer Nanocomposites Physics and Applications of Graphene*, Intech, 2011.

[19] J. A. King, D. R. Klimek, I. Miskioglu, and G. M. Odegard, "Mechanical properties of graphene nanoplatelet/epoxy composites," *Journal of Applied Polymer Science*, vol. 128, no. 6, pp. 4217–4223, 2013.

[20] F. Hussain, M. Hojjati, M. Okamoto, and R. E. Gorga, "Review article: polymer-matrix nanocomposites, processing, manufacturing, and application: an overview," *Journal of Composite Materials*, vol. 40, no. 17, pp. 1511–1575, 2006.

[21] S. Das, A. S. Wajid, J. L. Shelburne, Y. C. Liao, and M. J. Green, "Localized in situ polymerization on graphene surfaces for stabilized graphene dispersions," *ACS Applied Materials & Interfaces*, vol. 3, no. 6, pp. 1844–1851, 2011.

[22] J. H. Du, J. Bai, and H. M. Cheng, "The present status and key problems of carbon nanotube based polymer composites," *Express Polymer Letters*, vol. 1, no. 5, pp. 253–273, 2007.

[23] M. Moazzami Gudarzi and F. Sharif, "Enhancement of dispersion and bonding of graphene-polymer through wet transfer of functionalized graphene oxide," *Express Polymer Letters*, vol. 6, no. 12, pp. 1017–1031, 2012.

[24] R. K. Layek and A. K. Nandi, "A review on synthesis and properties of polymer functionalized graphene," *Polymer*, vol. 54, no. 19, pp. 5087–5103, 2013.

[25] N. Saravanan, R. Rajasekar, S. Mahalakshmi, T. P. Sathishkumar, K. S. K. Sasikumar, and S. Sahoo, "Graphene and modified graphene-based polymer nanocomposites - a review," *Journal of Reinforced Plastics and Composites*, vol. 33, no. 12, pp. 1158–1170, 2014.

[26] T. Grieb, K. Müller, O. Rubel et al., "Determination of nitrogen concentration in dilute GaNAs by STEM HAADF Z-contrast imaging," *Journal of Physics: Conference Series*, vol. 326, 2011.

[27] S. Kret, P. Ruterana, A. Rosenauer, and D. Gerthsen, "Extracting quantitative information from high resolution electron microscopy," *Physica Status Solidi (b)*, vol. 227, no. 1, pp. 247–295, 2001.

[28] S. I. Molina, M. P. Guerrero, P. L. Galindo, D. L. Sales, M. Varela, and S. J. Pennycook, "Calculation of integrated intensities in aberration-corrected Z-contrast images," *Journal of Electron Microscopy*, vol. 60, no. 1, pp. 29–33, 2011.

[29] F. Song, X. Wang, R. C. Powles et al., "Calibrating the atomic balance by carbon nanoclusters," *Applied Physics Letters*, vol. 96, no. 3, article 33103, 2010.

[30] R. Zan, U. Bangert, Q. Ramasse, and K. S. Novoselov, "Evolution of gold nanostructures on graphene," *Small*, vol. 7, no. 20, pp. 2868–2872, 2011.

[31] S. R. Plant, L. Cao, F. Yin, Z. W. Wang, and R. E. Palmer, "Size-dependent propagation of au nanoclusters through few-layer graphene," *Nanoscale*, vol. 6, no. 3, pp. 1258–1263, 2014.

[32] B. Goris, T. Roelandts, K. J. Batenburg, H. Heidari Mezerji, and S. Bals, "Advanced reconstruction algorithms for electron tomography: from comparison to combination," *Ultramicroscopy*, vol. 127, pp. 40–47, 2013.

[33] B. D. A. Levin, E. Padgett, C. C. Chen et al., "Nanomaterial datasets to advance tomography in scanning transmission electron microscopy," *Scientific Data*, vol. 3, p. 160041, 2016.

[34] R. Sengupta, M. Bhattacharya, S. Bandyopadhyay, and A. K. Bhowmick, "A review on the mechanical and electrical properties of graphite and modified graphite reinforced polymer composites," *Progress in Polymer Science*, vol. 36, no. 5, pp. 638–670, 2011.

[35] K. Nakada and A. Ishii, "Migration of adatom adsorption on graphene using DFT calculation," *Solid State Communications*, vol. 151, no. 1, pp. 13–16, 2011.

[36] I. F. Herbut, V. Juricic, and O. Vafek, "Relativistic Mott criticality in graphene," *Physical Review B*, vol. 80, no. 7, 2009.

[37] P. K. Chu and L. Li, "Characterization of amorphous and nanocrystalline carbon films," *Materials Chemistry and Physics*, vol. 96, no. 2-3, pp. 253–277, 2006.

[38] C. Walker, "Diamond coatings are branching out," *Physics World*, vol. 22, no. 8, pp. A15–A16, 2009.

[39] J. Pizarro, P. L. Galindo, E. Guerrero et al., "Simulation of high angle annular dark field scanning transmission electron microscopy images of large nanostructures," *Applied Physics Letters*, vol. 93, no. 15, p. 153107, 2008.

[40] E. J. Kirkland, *Advanced Computing in Electron Microscopy*, Springer, Boston, MA, 2010.

[41] http://www2.uca.es/serv/supercomputacion/.

[42] X. Ke, C. Bittencourt, and G. van Tendeloo, "Possibilities and limitations of advanced transmission electron microscopy for carbon-based nanomaterials," *Beilstein Journal of Nanotechnology*, vol. 6, pp. 1541–1557, 2015.

[43] https://imagej.nih.gov/ij/.

[44] P. Gilbert, "Iterative methods for the three-dimensional reconstruction of an object from projections," *Journal of Theoretical Biology*, vol. 36, no. 1, pp. 105–117, 1972.

[45] B. Goris, W. van den Broek, K. J. Batenburg, H. Heidari Mezerji, and S. Bals, "Electron tomography based on a total variation minimization reconstruction technique," *Ultramicroscopy*, vol. 113, pp. 120–130, 2012.

[46] C. MessaoudiI, T. Boudier, C. Sorzano, and S. Marco, "TomoJ: tomography software for three-dimensional reconstruction in transmission electron microscopy," *BMC Bioinformatics*, vol. 8, no. 1, p. 288, 2007.

[47] C. Li, W. Yin, H. Jiang, and Y. Zhang, "An efficient augmented Lagrangian method with applications to total variation minimization," *Computational Optimization and Applications*, vol. 56, no. 3, pp. 507–530, 2013.

[48] W. van Aarle, W. J. Palenstijn, J. de Beenhouwer et al., "The ASTRA toolbox: a platform for advanced algorithm development in electron tomography," *Ultramicroscopy*, vol. 157, pp. 35–47, 2015.

[49] S. G. Prolongo, R. Moriche, M. Sánchez, and A. Ureña, "Self-stratifying and orientation of exfoliated few-layer graphene nanoplatelets in epoxy composites," *Composites Science and Technology*, vol. 85, pp. 136–141, 2013.

[50] Z. Xu and C. Gao, "Graphene fiber: a new trend in carbon fibers," *Materials Today*, vol. 18, no. 9, pp. 480–492, 2015.

[51] H. Le Ferrand, S. Bolisetty, A. F. Demirörs, R. Libanori, A. R. Studart, and R. Mezzenga, "Magnetic assembly of transparent and conducting graphene-based functional composites," *Nature Communications*, vol. 7, 2016.

[52] M. Mahmoodi, M. Arjmand, U. Sundararaj, and S. Park, "The electrical conductivity and electromagnetic interference shielding of injection molded multi-walled carbon nanotube/polystyrene composites," *Carbon*, vol. 50, no. 4, pp. 1455–1464, 2012.